Reprinted from

JAPANESE JOURNAL OF
APPLIED
PHYSICS

REGULAR PAPER

Optimization of Correlation Kernel Size for Accurate Estimation of Myocardial Contraction and Relaxation

Yasunori Honjo, Hideyuki Hasegawa, and Hiroshi Kanai

Jpn. J. Appl. Phys. **51** (2012) 07GF06

© 2012 The Japan Society of Applied Physics

Person-to-person distribution (up to 10 persons) by the author only. Not permitted for publication for institutional repositories or on personal Web sites.

Japanese Journal of Applied Physics **51** (2012) 07GF06 **REGULAR PAPER**
DOI: 10.1143/JJAP.51.07GF06

Optimization of Correlation Kernel Size for Accurate Estimation of Myocardial Contraction and Relaxation

Yasunori Honjo[1], Hideyuki Hasegawa[1,2], and Hiroshi Kanai[1,2]*

[1] *Graduate School of Biomedical Engineering, Tohoku University, Sendai 980-8579, Japan*
[2] *Graduate School of Engineering, Tohoku University, Sendai 980-8579, Japan*

Received November 18, 2011; accepted April 19, 2012; published online July 20, 2012

For noninvasive and quantitative measurements of global two-dimensional (2D) heart wall motion, speckle tracking methods have been developed and applied. In these conventional methods, the frame rate is limited to about 200 Hz, corresponding to the sampling period of 5 ms. However, myocardial function during short periods, as obtained by these conventional speckle tracking methods, remains unclear owing to low temporal and spatial resolutions of these methods. Moreover, an important parameter, the optimal kernel size, has not been thoroughly investigated. In our previous study, the optimal kernel size was determined in a phantom experiment under a high signal-to-noise ratio (SNR), and the determined optimal kernel size was applied to the *in vivo* measurement of 2D displacements of the heart wall by block matching using normalized cross-correlation between RF echoes at a high frame rate of 860 Hz, corresponding to a temporal resolution of 1.1 ms. However, estimations under low SNRs and the effects of the difference in echo characteristics, i.e., specular reflection and speckle-like echoes, have not been considered, and the evaluation of accuracy in the estimation of the strain rate is still insufficient. In this study, the optimal kernel sizes were determined in a phantom experiment under several SNRs and, then, the myocardial strain rate was estimated such that the myocardial function can be measured at a high frame rate. In a basic experiment, the optimal kernel sizes at depths of 20, 40, 60, and 80 mm yielded similar results: in particular, SNR was more than 15 dB. Moreover, it was found that the kernel size at the boundary must be set larger than that at the inside. The optimal sizes of the correlation kernel were seven times and four times the size of the point spread function around the boundary and inside the silicone rubber, respectively. To compare the optimal kernel sizes, which was determined in a phantom experiment, with other sizes, the radial strain rates estimated using different kernel sizes were examined using the normalized mean-squared error of the estimated strain rate from the actual one obtained by the 1D phase-sensitive method. Compared with conventional kernel sizes, this result shows the possibility of the proposed correlation kernel to enable more accurate measurement of the strain rate. In *in vivo* measurement, the regional instantaneous velocities and strain rates in the radial direction of the heart wall were analyzed in detail at an extremely high temporal resolution (frame rate of 860 Hz). In this study, transition in contraction and relaxation was able to be detected by 2D tracking. These results indicate the potential of this method in the high-accuracy estimation of the strain rates and detailed analyses of the physiological function of the myocardium.
© 2012 The Japan Society of Applied Physics

1. Introduction

Myocardial strain and strain rate have been shown to be useful in estimating myocardial function, such like contraction and relaxation.[1–5] In recent years, there have been many studies on the measurement of two-dimensional (2D) myocardial strain or strain rate obtained by speckle tracking, which is direct tracking of backscattered echoes using regional pattern-matching techniques.[6–9] However, the frame rate (*FR*) in conventional speckle tracking methods is limited to about 200 Hz, corresponding to the sampling period of 5 ms.[10–13] Conventional speckle tracking methods at low temporal resolution may fail in estimating the heart wall motion because it leads to large changes in echo patterns (decorrelation) owing to the motion in the elevation direction.[14] In addition, in the period of one transition in myocardial contraction/relaxation, the heart wall moves rapidly during a short period of about 10 ms.[4] Therefore, the detailed analysis of the heart function has been limited owing to the low temporal resolution of conventional speckle tracking methods. The continuous observation of such rapid heart wall motion requires a high temporal resolution of more than 500 Hz.[1,4]

Moreover, the accuracy of the velocity and displacement estimated by the speckle tracking method depends on an important parameter, i.e., the size of the correlation kernel. To track backscattered echoes accurately, it is necessary to determine the optimal kernel size. Kaluzynski *et al.* reported that a silicone tube, with a diameter of 31 mm could be measured by tracking echoes from scatterers by correlation with a correlation kernel size of (1.0 laterally $\times$ 0.5 axially) mm^2.[15] Similarly, Bohs *et al.* accurately determined the velocity of a string phantom, which moves two-dimensionally at velocities up to 2.5 m/s, with a correlation kernel size of (1.0×2.0) mm^2. The blood flow in the lateral direction was imaged in *in vitro* experiments using a correlation kernel size of (0.8×0.8) mm^2.[16] By *in vivo* measurements for estimating the velocity and displacement spontaneously caused by the heart wall motion, the kernel size was determined to be (10.0×10.0) mm^2 by examining several kernel sizes in comparison with manual observation.[17–21] However, the optimal kernel size has not yet been thoroughly investigated.

In our previous study, the optimal kernel size was determined in a phantom experiment under a high signal-to-noise ratio (SNR), and the determined optimal kernel size was applied to the *in vivo* measurement of 2D displacements of the heart wall by block matching using a normalized cross-correlation between RF echoes at a high frame rate of 860 Hz, corresponding to a temporal resolution of 1.1 ms.[22] However, estimations under low SNRs and the effects of the difference in echo characteristics, i.e., specular reflection and speckle-like echoes, have not been considered, and the evaluation of the accuracy of an estimation of the strain rate is still insufficient. In this study, the optimal kernel sizes were determined in a phantom experiment under several SNRs and positions. The determined optimal kernel size was compared with conventional sizes in the evaluation of the accuracy in the estimation of the strain rate and, then, myocardial strain rate was estimated so that the myocardial function can be measured at a high frame rate.

*E-mail address: kanai@ecei.tohoku.ac.jp

 © 2012 The Japan Society of Applied Physics

Person-to-person distribution (up to 10 persons) by the author only. Not permitted for publication for institutional repositories or on personal Web sites.

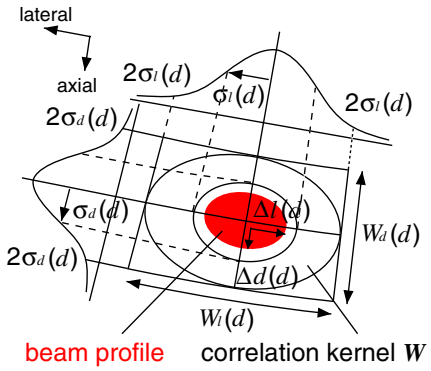

Fig. 1. (Color online) Schematic of correlation kernel ($W_l(d) \times W_d(d)$).

2. Principles

2.1 Definition of correlation kernel

In this study, 2D velocities and displacements of the heart wall are estimated by speckle tracking using the normalized cross-correlation function between RF echoes. Speckle size depends on the width of the ultrasonic beam and pulse length.[14,23] In this study, the size of the correlation kernel in the lateral direction $W_l(d)$ and that in the axial direction $W_d(d)$ were defined using the -20 dB widths of the lateral profile of the ultrasonic field $\Delta l(d)$ and the envelope of the ultrasonic pulse $\Delta d(d)$ at several depths, respectively. As illustrated in Fig. 1, the shape of the correlation kernel was a bivariate normal distribution. The variances $\sigma_l^2(d)$ and $\sigma_d^2(d)$ of the normal distribution in the lateral and axial directions were determined from the size of the point spread function (PSF) (lateral $\times$ axial) $= (\Delta l(d) \times \Delta d(d))$ and the variable coefficient α, respectively.[22]

2.2 Calculation of 2D velocities and radial strain rate

The lateral velocity $v_l(l,d;n)$ and axial velocity $v_d(l,d;n)$ between the n-th and $(n+\Delta N_{\mathrm{F}})$-th frames at a spatial point (l,d) (l: lateral, d: axial positions) in a heart wall are given by the determined lateral shift $\Delta\widehat{m}_n$ and axial shift $\Delta\widehat{k}_n$, respectively, which maximize the interpolated normalized cross-correlation function as follows:[22,24]

$$v_l(l,d;n) = \frac{\Delta\widehat{m}_n \cdot (\delta l/M_l)}{\Delta N_{\mathrm{F}} \cdot \Delta T} \quad (\mathrm{mm/s}), \tag{2.1}$$

$$v_d(l,d;n) = \frac{\Delta\widehat{k}_n \cdot (\delta d/M_d)}{\Delta N_{\mathrm{F}} \cdot \Delta T} \quad (\mathrm{mm/s}), \tag{2.2}$$

where ΔT and δl are the time interval between consecutive frames and the lateral spacing $\delta l = 2d \cdot \sin(\delta\theta/2)$ ($\delta\theta$: angular interval) of beams at depth d, respectively, and ΔN_{F} is the frame interval for the calculation of correlation. In this study, the normalized cross-correlation function was interpolated by reconstructive interpolation[24] to improve the accuracy in the estimation of the velocity and displacement.[22] The M_l and M_d are the interpolation factors in the lateral and axial directions, respectively.

We introduced the strain rate to evaluate how the thickness of each layer changes with respect to time. As shown in Fig. 2(a), the velocity in the radial direction, $v_r(r_i,\theta_j;n)$, which was calculated from the velocity in the lateral direction, $v_l(l,d;n)$, and that in the axial direction, $v_d(l,d;n)$, is given by

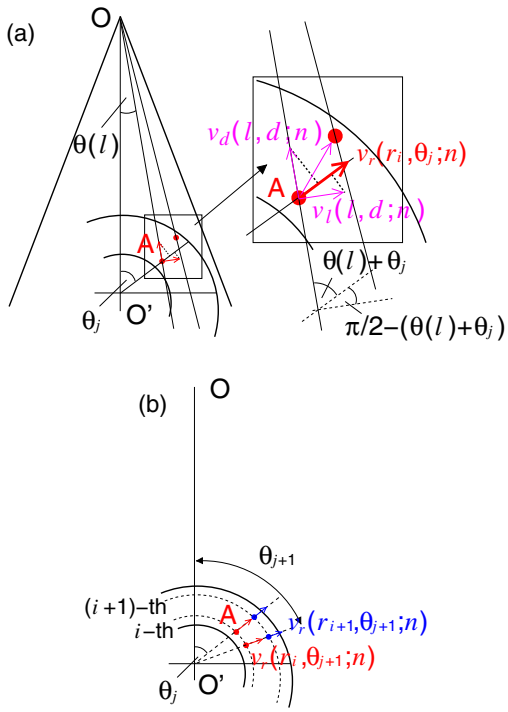

Fig. 2. (Color online) Schematic of calculation of radial strain rate.

$$v_r(r_i,\theta_j;n) = v_l(l,d;n)\cdot\sin[\theta_j+\theta(l)] + v_d(l,d;n)\cdot\cos[\theta_j+\theta(l)] \quad (\mathrm{mm/s}), \tag{2.3}$$

where θ_j and $\theta(l)$ are $\angle \mathrm{OO'A}$ and $\angle \mathrm{O'OA}$ in Fig. 2, respectively. As shown in Fig. 2(b), strain rate in the radial direction, $S_r(i,\theta_j;n)$, between the i-th and $(i+1)$-th layer is given by

$$S_r(r_i,\theta_j;n) = \frac{v_r(r_{i+1},\theta_j;n) - v_r(r_i,\theta_j;n)}{R} \quad [(\mathrm{mm/s})/\mathrm{mm}], \tag{2.4}$$

$$R = r_{i+1} - r_i, \tag{2.5}$$

where i and j are the numbers of layers and directions, respectively. The numerator shows the difference between velocities at positions (r_{i+1},θ_j) and (r_i,θ_j). The denominator R shows the initial thickness of the layer for the normalization of the velocity difference. After the strain rates were estimated at each radial position, they were superimposed on the B-mode image in every frame using a color code to obtain the 2D spatial distribution of the strain rate.

3. Determination of Optimal Size of Correlation Kernel by Basic Experiment

3.1 Measurement of the size of point spread function

In the present study, the kernel size was defined as a multiple of the size of PSF ($\Delta l(d) \times \Delta d(d)$) at each depth d, as $(\alpha\Delta l(d), \alpha\Delta d(d))$. The size of PSF is determined by the widths, at -20 dB, of the lateral profile of the ultrasonic field and the envelope of an ultrasonic echo obtained from experiments using a fine nylon wire (diameter: 31 µm) placed at depths of 20, 40, 60, and 80 mm. RF data were acquired using a 3.75 MHz sector-type probe of ultrasonic diagnostic equipment (Aloka α-10). In this study, plane waves were transmitted in $N_{\mathrm{t}} = 7$ different directions at angular intervals of 6° at a pulse repetition frequency f_{PRF} of

© 2012 The Japan Society of Applied Physics

Person-to-person distribution (up to 10 persons) by the author only. Not permitted for publication for institutional repositories or on personal Web sites.

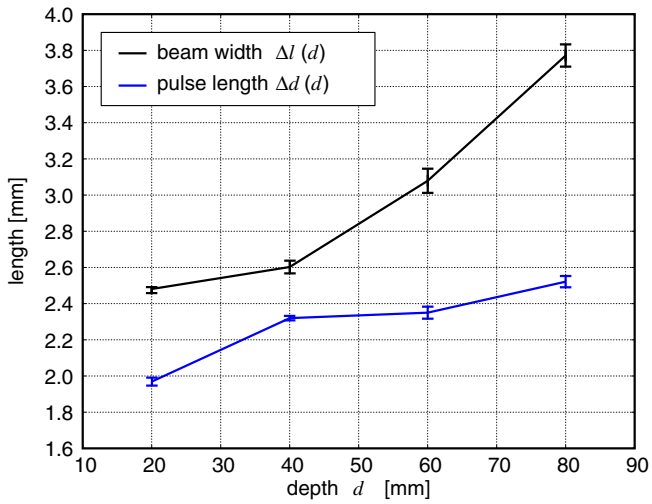

Fig. 3. (Color online) Distribution of −20 dB widths of lateral amplitude profile Δl and pulse envelope Δd of ultrasonic pulse at depths of 20, 40, 60, and 80 mm.

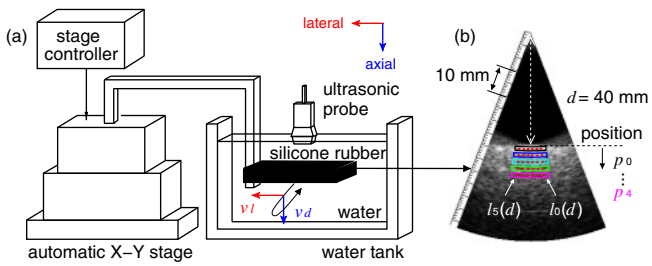

Fig. 4. (Color online) Schematic of phantom experiment to determine the optimal kernel sizes ($W_{l0}(d) \times W_{d0}(d)$).

6020 Hz using a 3.75 MHz sector-type probe. For each transmission, $N_r = 16$ receiving beams were created at angular intervals of $\delta\theta = 0.375°$. The *FR* obtained by parallel beam forming (PBF)[25] was $FR = f_{PRF}/N_t = 860$ Hz. The sampling frequency of the RF signal was 15 MHz. Figure 3 shows the size of PSF ($\Delta l(d) \times \Delta d(d)$) measured at different depths. The error bars show the standard deviation for five measurements at each depth d.

3.2 Basic experimental system

Figure 4 shows the basic experimental system. The motion of a phantom was measured to determine the optimum kernel size ($W_{l0}(d) \times W_{d0}(d)$). The phantom was made from silicone rubber (Momentive Performance Materials TSE3503) containing 5% graphite powder by weight to provide sufficient scattering. The phantom was set at the depths $\{d\}$ where the size of the PSF were measured. In this cross-sectional image of silicone rubber, the silicone rubber at the red points was analyzed. There were six beams l_i set at intervals from 41 ($i = 0$) to 71 ($i = 5$). Positions (p_0–p_4) were set at intervals of 1.5 mm from the upper surface of the phantom, where the depths $\{d\}$ were set at 20, 40, 60, and 80 mm. The phantom was a silicone rubber plate (sound speed c_0: 990 m/s) with a thickness of 15 mm. The motion velocity of the silicone rubber was controlled by an automatic X–Y stage. The phantom was moved two-dimensionally. Both the lateral velocity $v_{l0}(l, d; n)$ and axial velocity $v_{d0}(l, d; n)$, which were set at a constant speed of

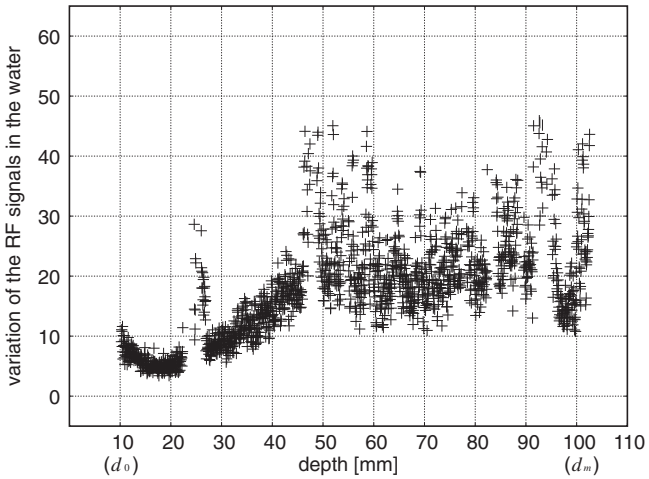

Fig. 5. Variance of RF signals in water.

5 mm/s, were smaller than those of the heart wall.[26] Therefore, the 2D displacements, $x_l(l, d; n)$ and $x_d(l, d; n)$, of the silicone rubber between two frames ΔN_F were respectively set to be similar to those of the heart wall by increasing the frame interval ΔN_F for calculating the correlation function.[22,26]

3.3 Calculation of signal-to-noise ratio

SNRs from the phantom placed in water are higher than those from the heart wall in *in vivo* measurement. Therefore, in this study, white noise was added to the RF signals $\{\mathrm{rf}(l, d)\}$ measured in the basic experiment so that SNR of echoes in the basic experiment became similar to those in the *in vivo* measurement. The white noise $\eta_w(l, d)$ was created by MATLAB (MathWorks). SNR of an echo signal from the phantom, which contains noise $\eta_0(l, d)$ originating from the ultrasonic equipment and $\eta_w(l, d)$, is given by

$$\begin{aligned}\mathrm{SNR} &= 10\log_{10}(\mathrm{E}_{(l,d)}[(\mathrm{E}_t[\mathrm{rf}(l,d)])^2]) \\ &\quad - 10\log_{10}(\mathrm{E}_{(l,d)}[(\eta_0(l,d) + \beta\cdot\eta_w(l,d))^2]) \\ &= 10\log_{10}(\mathrm{E}_{(l,d)}[(\mathrm{E}_t[\mathrm{rf}(l,d)])^2]) \\ &\quad - 10\log_{10}(\mathrm{E}_{(l,d)}[\eta_0(l,d)^2 + (\beta\cdot\eta_w(l,d))^2]), \qquad (3.1)\end{aligned}$$

where $\mathrm{E}_t[\cdot]$ and $\mathrm{E}_{(l,d)}[\cdot]$ are the time and space (lateral and axial directions) average operations, respectively, and β is the amplitude coefficient controlling SNR. There is no correlation between the noise $\eta_0(l, d)$ caused by the ultrasonic equipment and white noise $\eta_w(l, d)$, i.e., $\mathrm{E}_{(l,d)}[\eta_0(l, d)\cdot\eta_w(l, d)] = 0$. The SNRs in the basic experiment in the regions of p_j at depth d in Fig. 4(b) are given by

$$\begin{aligned}\mathrm{SNR}(p_j; d) &= 10\log_{10}\left[\frac{1}{A}\sum_{l=l_0}^{l_5}\left\{\frac{1}{N}\sum_{n=0}^{N-1}(\mathrm{rf}_n(l,d))\right\}^2\right] \\ &\quad - 10\log_{10}\left[\frac{1}{A}\sum_{l=l_0}^{l_5}\left\{(\mathrm{E}_t[\eta_0(l,d)^2]) \right.\right. \\ &\quad \left.\left. + \left(\frac{\beta}{N}\sum_{n=0}^{N-1}(\eta_w(l,d))^2\right)\right\}\right], \qquad (3.2)\end{aligned}$$

$$(A = l_5 - l_0), \qquad (3.3)$$

where j is the number of depths ($j = 0, 1, \cdots, 4$) set in the silicone rubber, as shown in Fig. 4. In this study, as shown in

© 2012 The Japan Society of Applied Physics

Person-to-person distribution (up to 10 persons) by the author only. Not permitted for publication for institutional repositories or on personal Web sites.

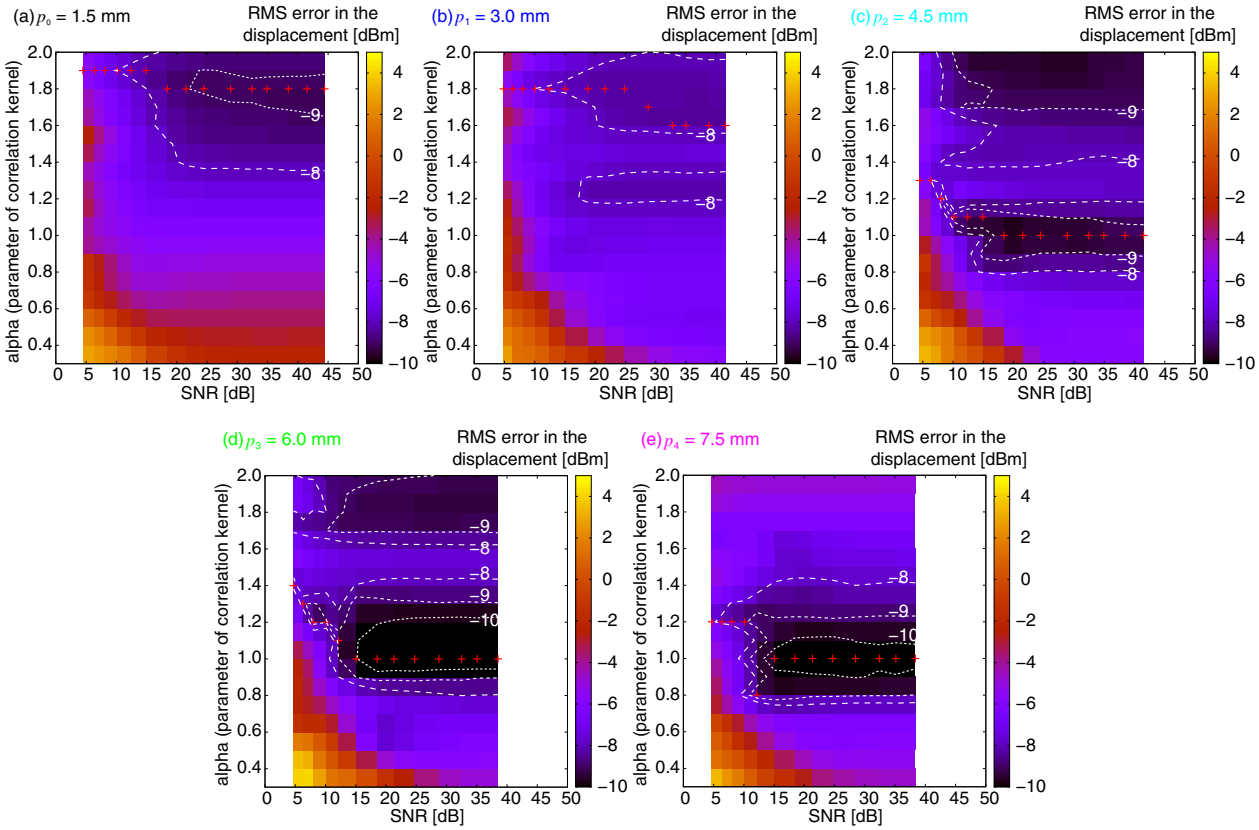

Fig. 6. (Color online) RMS errors $\{\epsilon(\alpha, \mathrm{SNR}(p_j; d), d)\}$ at the depth of 40 mm obtained as a function of the correlation window width coefficient α and SNR.

Fig. 5, the noise $\eta_0(l, d)$ was estimated as the variance of the output signal from the equipment, and was measured without any objects in water, as follows:

$$\eta_0(l, d)^2 = \frac{1}{N}\sum_{n=0}^{N-1}(\mathrm{rf}_n(l, d) - \overline{\mathrm{rf}}(l, d))^2, \tag{3.4}$$

$$\overline{\mathrm{rf}}(l, d) = \frac{1}{N}\sum_{n=0}^{N-1}\mathrm{rf}_n(l, d), \tag{3.5}$$

where N is the number of frames used in the calculation of the variance.

3.4 Determination of the optimal size of correlation kernel

In this study, the sizes $W_l(d)$ and $W_d(d)$ of the correlation kernel in the lateral and axial directions were defined by $\pm 2\sigma_l$ $(= \pm 2\alpha \cdot \Delta l(d))$ and $\pm 2\sigma_d$ $(= \pm 2\alpha \cdot \Delta d(d))$, respectively. To determine the optimal value $\alpha_{\mathrm{opt}}(d, \mathrm{SNR}(p_j; d))$ of α giving the optimal kernel size $(W_{l0}(d) \times W_{d0}(d))$, the 2D displacements of the phantom estimated using different values of $\{\alpha\}$ and SNRs were examined using the root-mean-squared (RMS) error of the estimated displacement from the actual displacement. The RMS errors in the estimated 2D displacements, $\{\epsilon(\alpha, \mathrm{SNR}(p_j; d), d)\}$, which were evaluated for each value of α and $\mathrm{SNR}(p_j; d)$ at depth d, were calculated from the lateral displacement $x_l(l_i, d; n)$ and axial displacement $x_d(l_i, d; n)$ estimated for each position (l_i, d) and the actual lateral displacement $x_{l0}(n)$ and axial displacement $x_{d0}(n)$ as follows:

$$\epsilon(\alpha, \mathrm{SNR}(p_j; d), d) = \sqrt{\frac{1}{I \cdot N}\sum_{i=0}^{5}\sum_{n=0}^{N-1}(\Delta x_l(l_i, d; n)^2 + \Delta x_d(l_i, d; n)^2)}, \tag{3.6}$$

$$\Delta x_l(l_i, d; n) = x_l(l_i, d; n) - x_{l0}(n), \tag{3.7}$$

$$\Delta x_d(l_i, d; n) = x_d(l_i, d; n) - x_{d0}(n), \tag{3.8}$$

where N and I $(= 6)$ are the numbers of averaged frames and measurement points, respectively. In this experiment, the displacements at the position $\{(l_i, d)\}$ in the area of 2D tracking were measured using normalized cross-correlation functions with different values of $\alpha = 0.3 - 2.0$ at the five positions (p_0–p_4) at each depth of 20, 40, 60, and 80 mm. The original sampled normalized cross-correlation function was interpolated with $M_l = 120$ in the lateral direction and $M_d = 15$ in the axial direction to obtain the cross-correlation function with similar resolutions in the lateral and axial directions, corresponding to 2.2 µm.

Figure 6 shows the distributions of RMS errors, $\{\epsilon(\alpha, \mathrm{SNR}(p_j; d), d)\}$, estimated using different values of $\{\alpha\}$ of the correlation kernels at the five positions [(a) $p_0 = 1.5$ mm – (e) $p_4 = 7.5$ mm]. As shown in Fig. 6, when the size of the correlation kernel is set to be small,

© 2012 The Japan Society of Applied Physics

Person-to-person distribution (up to 10 persons) by the author only. Not permitted for publication for institutional repositories or on personal Web sites.

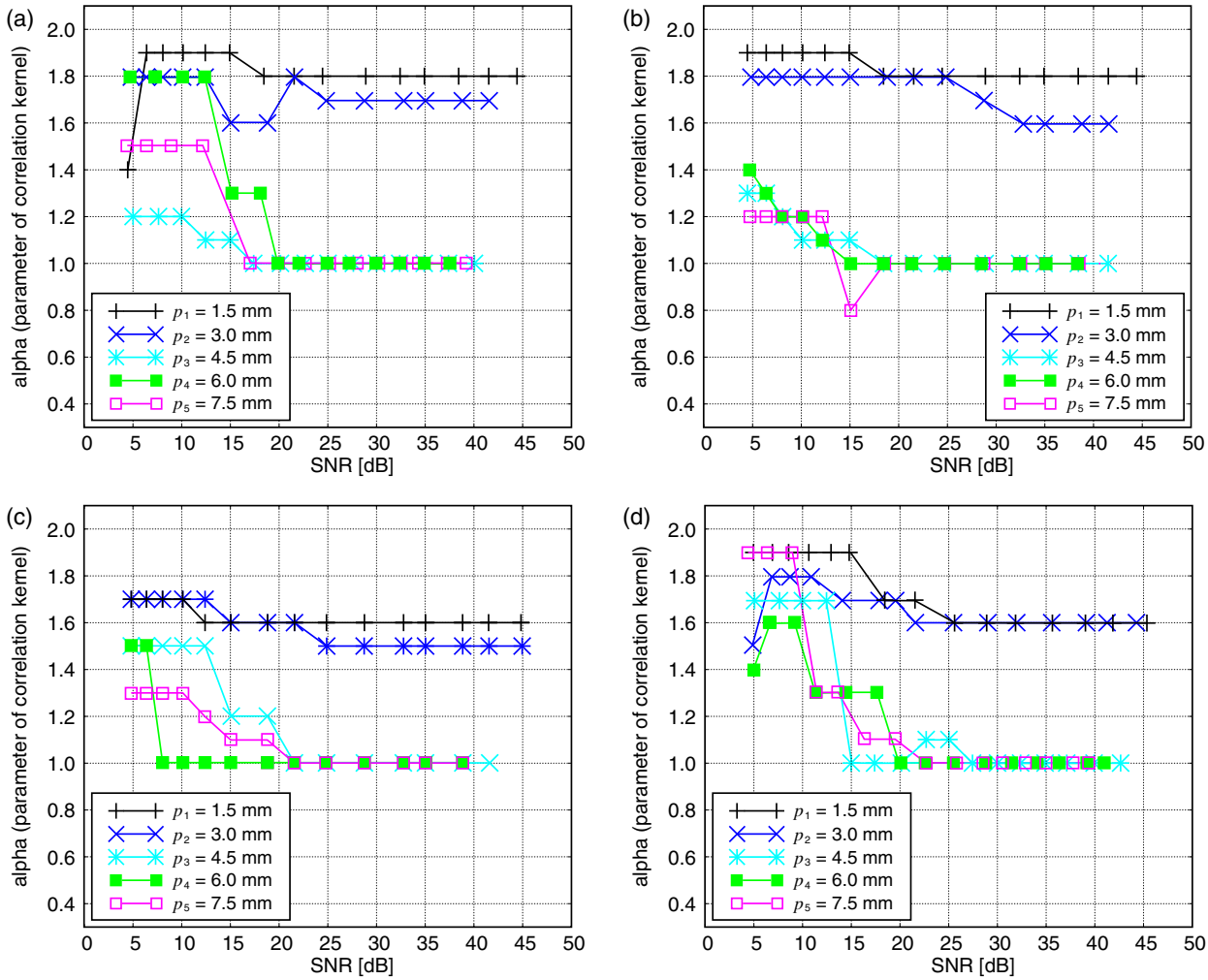

Fig. 7. (Color online) Optimal values of $\alpha_{\mathrm{opt}}(d, \mathrm{SNR}(p_j; d))$ plotted as a function of SNR for five positions (p_0–p_4) at each depth d ($d = 20$, 40, 60, and 80 mm).

there may be several regions in the next frame that have echo patterns similar to those in the small correlation kernel in the previous frame. These multiple regions, which have similar echo patterns, induce misestimation of displacement. When the size of the kernel is set to be too large, the peak of the correlation coefficient is degraded because the speckle pattern of the central position in the correlation kernel is different from that of the edge in the correlation kernel, owing to deflection of the ultrasonic beam. In addition, it is rare that the echo patterns in the two frames exactly coincide, which degrades the accuracy of the estimation and the spatial resolution.[27–29] However, the displacement estimation is less susceptible to noise because the echo pattern in the correlation kernel is more unique.

Figures 7(a)–7(d) show the relationships among the SNRs $\{\mathrm{SNR}(p_j; d)\}$ $(j = 0, 1, 2, 3, 4)$, the values of $\{\alpha_{\mathrm{opt}}(d, \mathrm{SNR}(p_j; d))\}$, which are the minimum RMS errors, and the positions $\{p_j\}$ at each depth d from the upper surface. As shown in Fig. 7, the distributions of the values of $\{\alpha_{\mathrm{opt}}(d, \mathrm{SNR}(p_j; d))\}$ at the positions of a boundary of the silicone rubber (p_0 and p_1) were different from those inside the silicone rubber (p_2–p_4). As shown in Fig. 4(b), the brightness is high and relatively uniform in the lateral direction at the boundary of the silicone rubber. In such cases, there might be several regions in the next frame that have echo patterns similar to those in the correlation kernel in the previous frame. Such a situation leads to the misestimation of displacement. Figures 8(a) and 8(b) show profiles of the normalized cross-correlation functions obtained for points of interest at the boundary (p_0) and inside (p_4) the silicone rubber, respectively. As shown in Fig. 8(a-1), at large α ($\alpha = 1.8, 2.0$), the profiles around the peak of the normalized cross-correlation functions in the lateral direction became narrower around the boundary of the silicone rubber (at p_0). On the other hand, as shown in Fig. 8(b-1), at $\alpha \simeq 1.0$, the profile around the peak of the normalized cross-correlation function in the lateral direction became narrowest inside the silicone rubber (at p_4). The profiles around the peaks of the normalized cross-correlation functions in the axial direction around the boundary and inside the silicone plate were similar, as shown in Figs. 8(a-2) and 8(b-2), respectively. Therefore, the kernel size at the boundary must be set larger than that inside.

As shown in Fig. 1, in our study, the correlation kernel was defined using the size of PSF ($\Delta l(d) \times \Delta d(d)$), and the optimal sizes $\{(W_{l0}(d) \times W_{d0}(d))\}$ were determined as $\pm 2 \cdot \alpha_{\mathrm{opt}}(d, \mathrm{SNR}(p_j; d))(\Delta l(d) \times \Delta d(d))$. As shown in Figs. 7(a)–7(d), when SNR is larger than 15 dB, the optimal

 © 2012 The Japan Society of Applied Physics

Person-to-person distribution (up to 10 persons) by the author only. Not permitted for publication for institutional repositories or on personal Web sites.

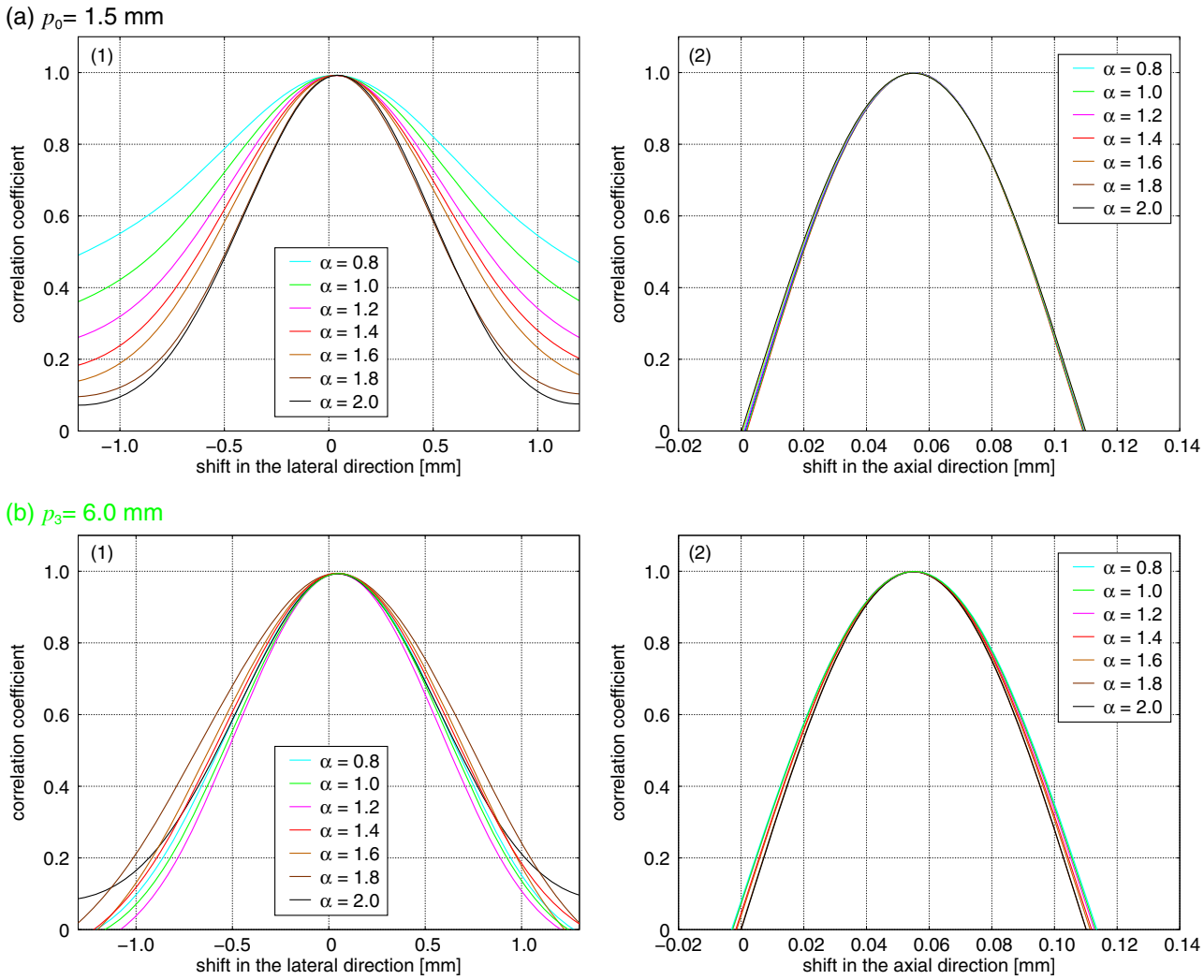

Fig. 8. (Color online) Distribution of correlation coefficient in the lateral (1) and axial (2) directions. (a) $p_0 = 1.5$ mm. (b) $p_3 = 6.0$ mm.

value of $\alpha_{\mathrm{opt}}(d, \mathrm{SNR}(p_j; d))$ at each depth d (= 20, 40, 60, and 80 mm) is 1.6–1.8 around the boundary and 1.0 inside the silicone rubber. From these results, the optimal kernel sizes $\{(\widehat{W}_{l0}(d) \times \widehat{W}_{d0}(d))\}$ were determined to be about seven times ($\pm 2 \cdot \alpha_{\mathrm{opt}}(\Delta l(d) \times \Delta d(d))$ ($\alpha_{\mathrm{opt}} = 1.6$–$1.8$)) and four times ($\pm 2 \cdot \alpha_{\mathrm{opt}}(\Delta l(d) \times \Delta d(d))$ ($\alpha_{\mathrm{opt}} = 1.0$)) the size of PSF ($\Delta l(d) \times \Delta d(d)$) around the boundary and inside the silicone rubber, respectively. It was found that the optimal kernel sizes $\{(W_{l0}(d) \times W_{d0}(d))\}$ can be determined from the size of PSF ($\Delta l(d) \times \Delta d(d)$), which is determined by the lateral and axial widths at a -20 dB ultrasonic field measured in advance.

4. Basic Experiment of Estimation of Radial Strain Rate

4.1 Experimental system

As illustrated in Fig. 9, in this experiment, the strain rate of the phantom owing to the change in the internal pressure, which was applied using a flow pump, was measured. The homogeneous cylindrical phantom with a wall thickness of 2 mm was made from silicone rubber. In this study, the RF data were acquired using the 3.75 MHz sector-type probe of ultrasonic diagnostic equipment (Aloka α-10). All parameters, sound speed c_0, the sampling frequency f_s of the RF signal, frame rate FR, and interpolation factors M_l and M_d in

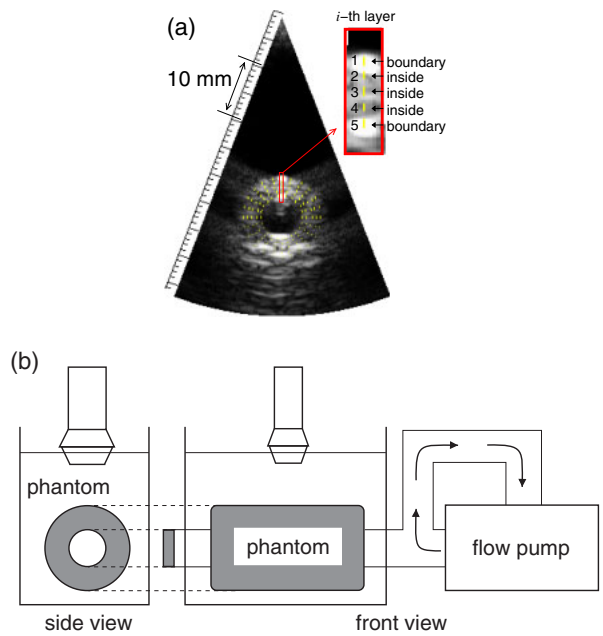

Fig. 9. (Color online) (a) Cross-sectional image of silicone tube at a depth of 40 mm. The yellow points in this cross-sectional image show positions $\{(l, d)\}$ for displacement estimation. (b) Schematic of phantom experiment to estimate the radial strain rates $\{S_r(r_i, \theta_j; n)\}$.

© 2012 The Japan Society of Applied Physics

Person-to-person distribution (up to 10 persons) by the author only. Not permitted for publication for institutional repositories or on personal Web sites.

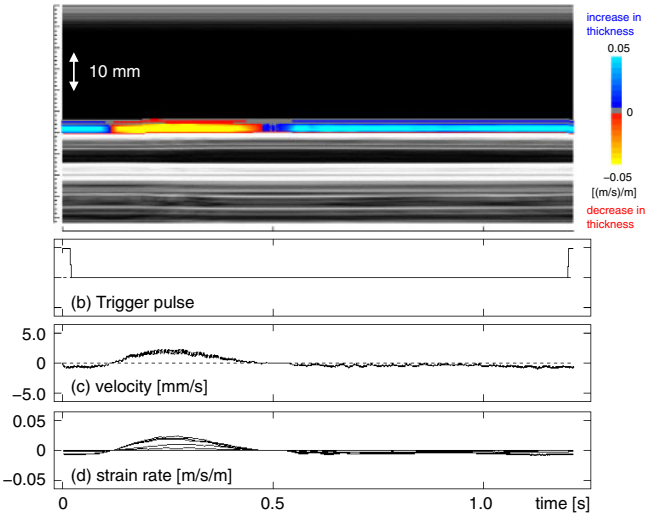

Fig. 10. (Color online) Actual strain rate $S_{r0}(r_i, \theta_j; n)$ of silicone tube along the central beam ($\theta_j = 0$) obtained by 1D phase-sensitive method.

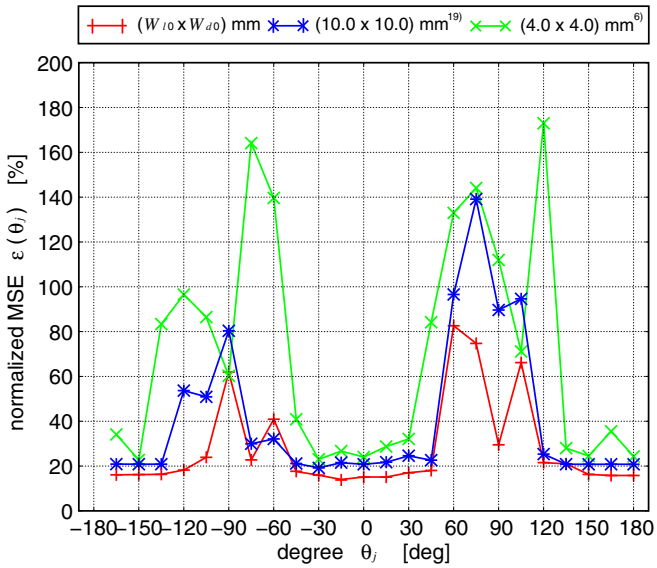

Fig. 11. (Color online) Distribution of MSEs $\{\epsilon(\theta_j)\}$ using different sizes of correlation kernels. (Red line) proposed optimal kernel size ($W_{l0} \times W_{d0}$). (Blue and green lines) conventional kernel sizes.

the lateral and axial direction, were the same as those used in the basic experiment using the silicone rubber. In this study, to obtain the actual velocity $v_{r0}(r_i, \theta_j; n)$ and strain rate $S_{r0}(r_i, \theta_j; n)$ in the phantom's radial direction, a 1D phase-sensitive method (1D method) was used for the central beam ($\theta_j = 0°$). The silicone rubber was assumed to be an isotropic medium in the circumferential direction. Therefore, the actual strain rate $S_{r0}(r_i, \theta_j; n)$ ($\theta_j = 0°$) obtained by the 1D method and shown in Fig. 10 can be used as references for all directions $\{\theta_j\}$ and layers $\{r_i\}$.

4.2 Experimental results

Some features of speckle patterns, such as the size of a speckle, depend on the PSF produced by the ultrasonic field.[14,23] In this study, the RF data were acquired using the 3.75 MHz sector-type probe of ultrasonic diagnostic equipment (Aloka α-10), which was the same as that used in the basic experiment so that the features of speckle size were not changed. Therefore, the size of a correlation kernel determined by the basic experiment was also used in this experiment. As illustrated in Fig. 9(a), the correlation kernel at the position of the boundaries (first and fifth layers) and inside (second, third, and fourth layers) the silicone rubber were set at seven times [$(18.2 \times 16.9)\,\mathrm{mm}^2$] and four times [$(10.4 \times 9.7)\,\mathrm{mm}^2$] the size of the PSF ($\Delta l \times \Delta d$), respectively.

To compare the optimal kernel size determined in the phantom experiment, with other sizes, the radial strain rates estimated using different kernel sizes were examined using the normalized mean-squared error (MSE) of the estimated strain rate $S_r(r_i, \theta_j; n)$ from the actual one $S_{r0}(r_i, \theta_j; n)$. The normalized mean-squared error $\epsilon(\theta_j)$ was calculated from the radial strain rate $S_r(r_i, \theta_j; n)$ at each position (r_i, θ_j) and actual $S_{r0}(r_i, \theta_j; n)$ as follows:

$$\epsilon(\theta_j) = \frac{\sum_{i=0}^{I-1}\sum_{n=0}^{N-1}(S_r(r_i, \theta_j; n) - S_{r0}(r_i, \theta_j; n))^2}{\sum_{i=0}^{I-1}\sum_{n=0}^{N-1}(S_{r0}(r_i, \theta_j; n))^2}, \quad (4.1)$$

where I and N are the number of layers and the number of frames, respectively. Figure 11 shows the distribution of MSEs, $\{\epsilon(\theta_j)\}$, estimated using different correlation kernel sizes[7,21] of $(4.0 \times 4.0)\,\mathrm{mm}^2$ and $(10 \times 10)\,\mathrm{mm}^2$ and proposed optimal kernel sizes corresponding to the sizes of $(18.2 \times 16.9)\,\mathrm{mm}^2$ and $(10.4 \times 9.7)\,\mathrm{mm}^2$, which were set at the boundary and inside the silicone rubber, respectively. The strain rates in the radial direction estimated with the proposed correlation kernel size yielded the least MSE. On the other hand, the strain rate estimated using the previously examined kernel sizes, (4.0×4.0) and $(10 \times 10)\,\mathrm{mm}^2$, were markedly different from the actual one. As shown in Fig. 11, MSEs $\{\epsilon(\theta_j)\}$ became smaller at around $\{\theta_j\}$ of 0 and $\pm 180°$. In contrast, MSEs $\{\epsilon(\theta_j)\}$ became larger at around $\{\theta_j\}$ of 90° because the component of the velocity in the lateral direction was larger than the axial one at around $\{\theta_j\}$ of 90°, and hence, the accuracy of the estimation of the velocity in the lateral direction was low. Compared with conventional kernel sizes, this result shows that the proposed correlation kernel size realizes more accurate measurement of the strain rate at the expense of the spatial resolution.

However, as shown in Fig. 11, the minimum MSE in the strain rate was about 20% because the instantaneous displacement (velocity $\times\, 1/FR$) of the silicone tube during two frames was very small. The maximum instantaneous displacement was 12 µm. The sampling intervals δl and δd of the correlation function in the lateral and axial directions after interpolation were both 2.2 µm at the depth d of 40 mm. Therefore, even if the error between estimated and actual displacement is minimum, corresponding to one point of the sampled correlation function, the error becomes about 20% [$= (2.2\,\mu\mathrm{m})/(12\,\mu\mathrm{m})$]. In future work, it is necessary to improve the spatial resolution of the ultrasound system by narrowing PSF, because the size of PSF, $(\Delta l(d) \times \Delta d(d)) = (2.48 \times 1.96)\,\mathrm{mm}^2$, at the depth d of 40 mm was much larger than the instantaneous displacement of the silicone tube.

© 2012 The Japan Society of Applied Physics

Person-to-person distribution (up to 10 persons) by the author only. Not permitted for publication for institutional repositories or on personal Web sites.

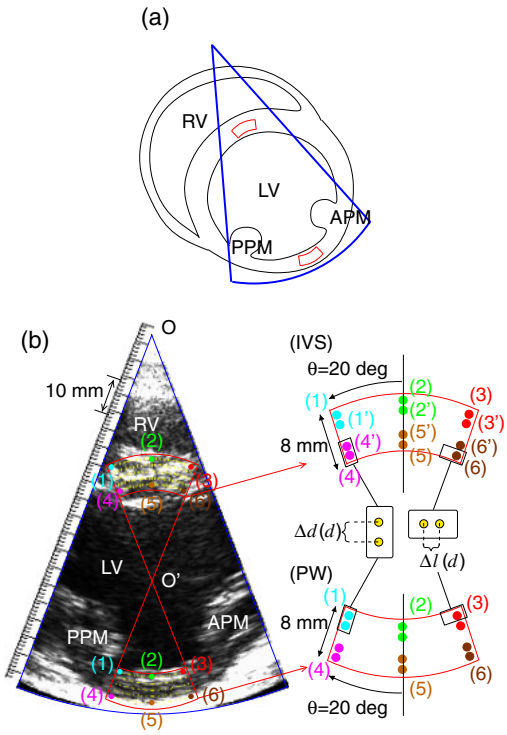

Fig. 12. (Color online) (a) Acquisition area of RF signals in the short-axis view. (b) 2D velocities and strain rate are estimated at the yellow points on the cross-sectional image of IVS and PW. The intervals of the points were set to be equivalent to the size of the point spread function ($\Delta l(d) \times \Delta d(d)$).

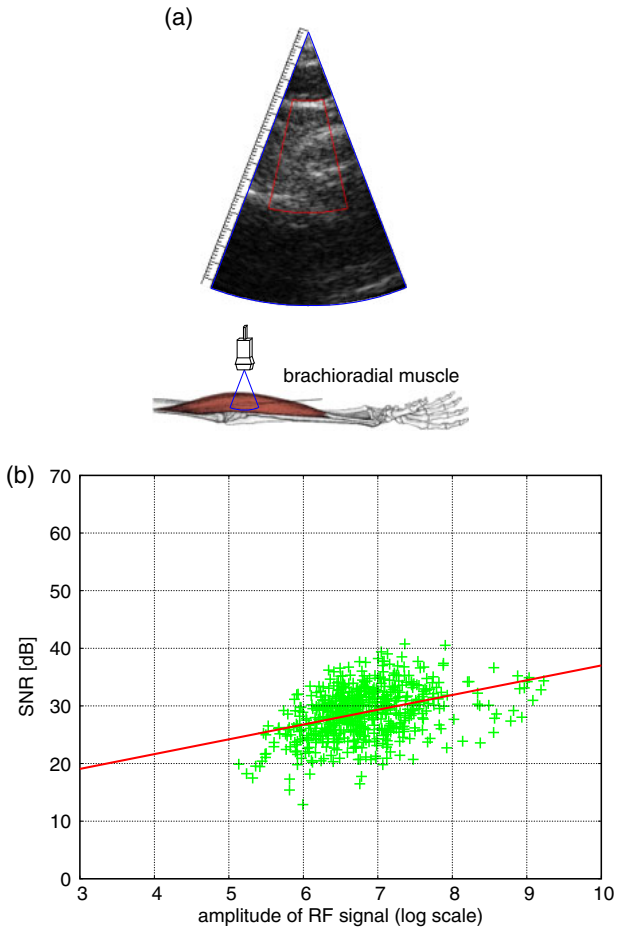

Fig. 13. (Color online) (a) Cross-sectional image of the brachioradial muscle. (b) Relationship between amplitude of RF signals and SNR.

5. *In vivo* Experimental Results

5.1 Acquisition of RF signals in interventricular septum

Figure 12 shows a typical cross-sectional image (short-axis view of left ventricle) of the heart obtained from a healthy 22-year-old male. Figure 12(a) shows the RF acquisition area. In the acquisition of RF signals, the ultrasonic beam scanned 112 different directions densely to maintain a high spatial resolution. The frame rate was set at 860 Hz. As shown in Fig. 12(b), the instantaneous velocities and strain rates of the regions in the interventricular septum (IVS) and posterior wall (PW) of the left ventricle were estimated by 2D tracking. The yellow points in this cross-sectional image show the positions $\{(l, d)\}$ of the points of interest, which were set at intervals of the PSF ($\Delta l(d) \times \Delta d(d)$).

5.2 Calculation of SNR in *in vivo* experiment

In this study, the RF data were acquired using the 3.75 MHz sector-type probe of ultrasonic diagnostic equipment, which was the same as that used in the basic experiment so that the features of speckle size were not changed. The correlation kernel sizes $\{(W_{l0}(d) \times W_d(d))\}$ at the depths of IVS and PW determined in the basic experiment were also used in the *in vivo* experiment. To determine the optimal kernel sizes from the data in Fig. 7, SNR in the *in vivo* experiment was estimated.

The heart wall continuously contracts and relaxes during a cardiac cycle. Therefore, it is difficult to calculate SNR directly in *in vivo* measurements. The SNRs in *in vivo* measurements were estimated by measuring another static muscle (brachioradial muscle). The relationship between SNRs and the power of the RF echo is obtained by the measurement of brachioradial muscle. As shown in Fig. 13, the SNR was calculated as the ratio of the power of the RF echo from the static brachioradial muscle (S), which was averaged for frames, and the variance $\eta_0(l, d)$ of the RF echoes (N), as in eq. (3.4). Then, the regression line describing the relationship between the SNR and the power of the echo is determined by the least-squares method. Using the determined regression line, the SNR in the *in vivo* measurement of the heart is estimated from the power of an echo from the heart wall, assuming that the relationship between the SNR and the power of the echo is the same in the measurements of brachioradial and heart muscles. The power $\mathrm{P_{PSF}}(i, j; n)$ of the RF echo $\mathrm{rf}_n(l, d) = \mathrm{rf}_n(i \cdot \delta l, j \cdot \delta d)$ in the region of the PSF ($\Delta l(d) \times \Delta d(d)$) in an *in vivo* measurement is given by

$$\mathrm{P_{PSF}}(i, j; n) = \log_{10}\left[\frac{1}{M}\sum_{b=-B/2}^{B/2}\sum_{k=-K/2}^{K/2}\{\mathrm{rf}_n((i + b + \Delta\widehat{m}_n) \cdot \delta l, (j + k + \Delta\widehat{k}_n) \cdot \delta d)\}^2\right], \tag{5.1}$$

$$(M = (B + 1)(K + 1), \Delta l = (B + 1) \cdot \delta l, \Delta d = (K + 1) \cdot \delta d), \tag{5.2}$$

© 2012 The Japan Society of Applied Physics

Person-to-person distribution (up to 10 persons) by the author only. Not permitted for publication for institutional repositories or on personal Web sites.

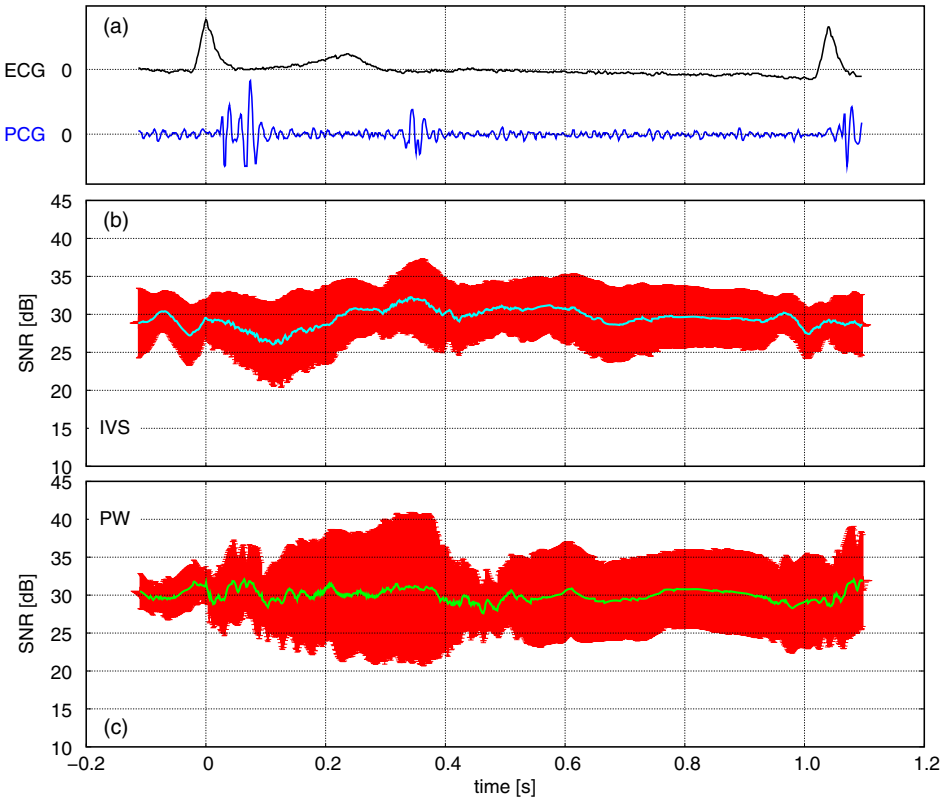

Fig. 14. (Color online) Calculation of the average SNR in a cardiac cycle in *in vivo* measurement. The red region is composed of many lines that show standard deviations in the respective frames. (a) Electrocardiogram and phonocardiogram. (b) IVS. (c) PW.

where B and K are the numbers of beams and sampling points in the PSF ($\Delta l(d) \times \Delta d(d)$), respectively. The $\Delta\widehat{m}_n$ and $\Delta\widehat{k}_n$ are the shifts in the lateral and axial directions, respectively, which maximize the interpolated normalized cross-correlation function. As shown in Fig. 14, the estimated SNRs in the *in vivo* measurement were more than 20 dB. This result shows that the sizes $\{(\widehat{W}_l(d) \times \widehat{W}_d(d))\}$ of the correlation kernel determined by the basic experiment were also used in the *in vivo* measurement, i.e., they were seven times [$\alpha_{\mathrm{opt}} = 1.6$ (IVS), 1.8 (PW)] and four times ($\alpha_{\mathrm{opt}} = 1.0$) the size of the PSF ($\Delta l(d) \times \Delta d(d)$) around the boundary and inside the heart wall, respectively.

5.3 Comparison of previous and proposed correlation kernels

As shown in Figs. 7 and 8, the correlation kernel size at the boundary must be set larger than that inside. However, in the previous study, the characteristics of echoes, i.e., specular reflection and speckle-like echoes, was not considered. Therefore, 2D displacements at the boundary of the heart wall estimated using the previous[22] and proposed correlation kernel sizes were compared.

The yellow points in Figs. 15(a) and 15(b) show the instantaneous displacement obtained using the previous and proposed correlation kernels. The previous and proposed optimal kernel sizes ($W_{l0}(d) \times W_{d0}(d)$) at the boundary of the heart wall correspond to four and seven times the size of the PSF ($\Delta l(d) \times \Delta d(d)$). Figures 15(a-1) and 15(b-1) show the same image, which is the first frame at the beginning of the R-wave. As shown in Figs. 15(a-2) and 15(b-2), the displacement in the axial direction was similar. However,

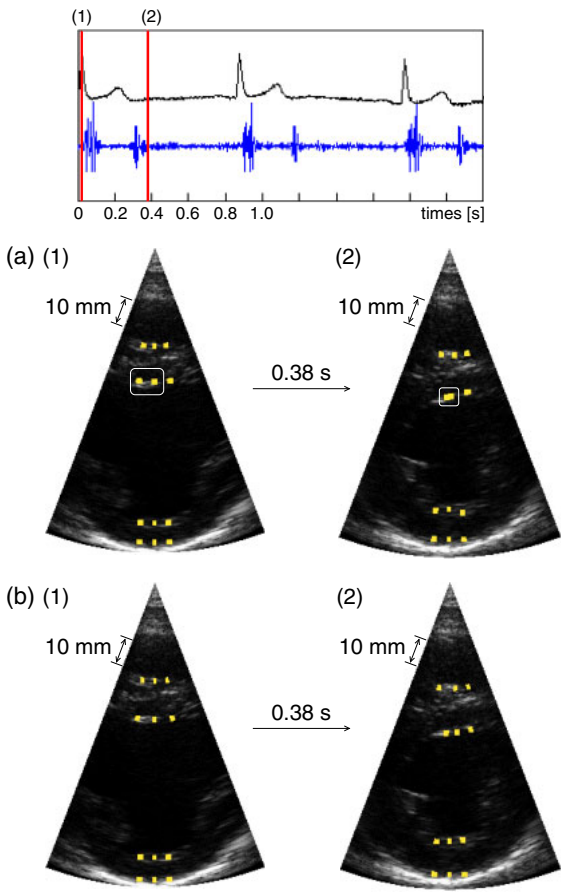

Fig. 15. (Color online) Results obtained using previous (a) and proposed (b) correlation kernels. The yellow points show the instantaneous positions of points of interest.

© 2012 The Japan Society of Applied Physics

Person-to-person distribution (up to 10 persons) by the author only. Not permitted for publication for institutional repositories or on personal Web sites.

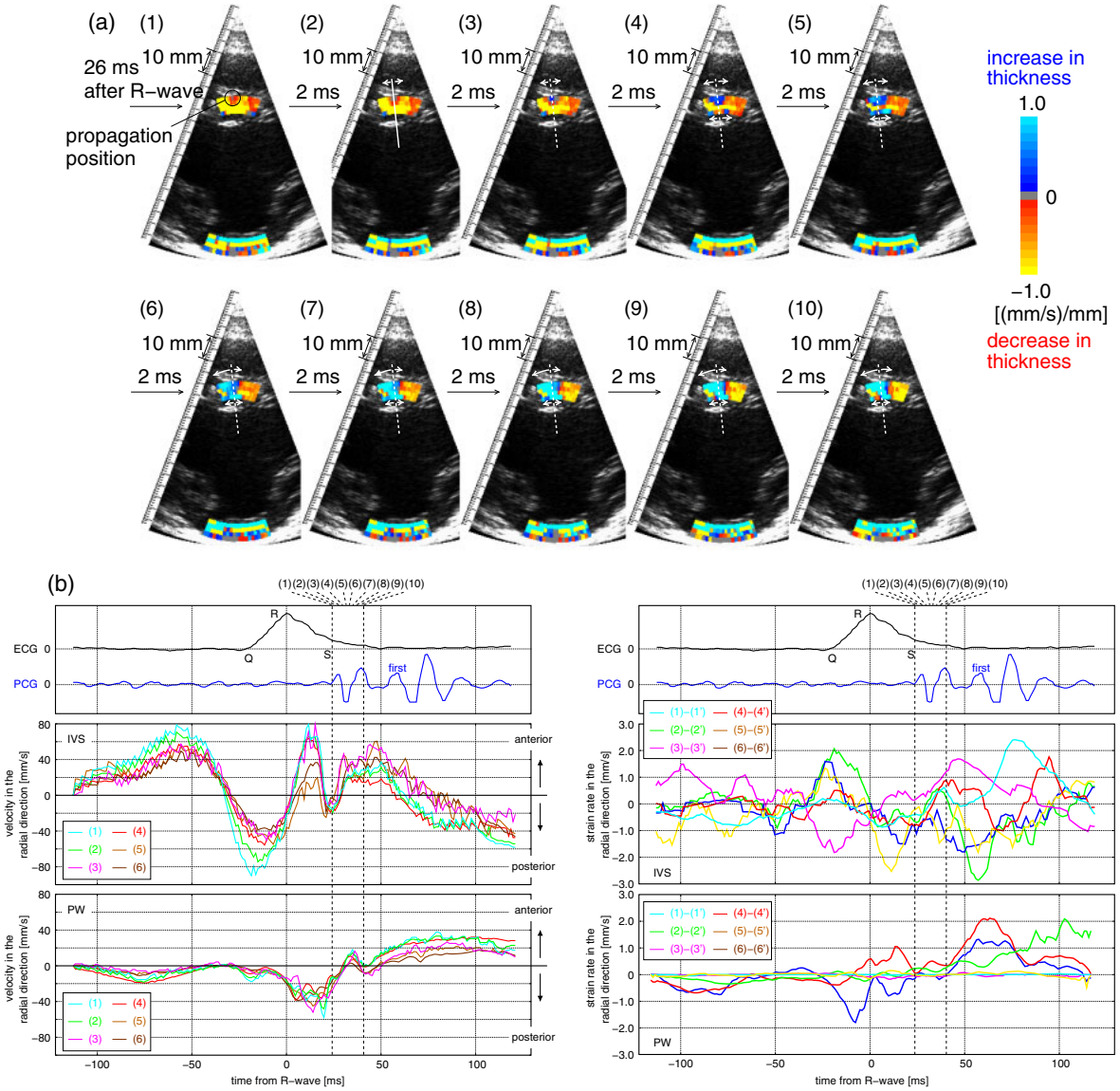

Fig. 16. (Color online) (a) Distributions of the strain rate in the radial direction around the R-wave. The cross-sectional images of the short-axis view of LV (1)–(10) were obtained every 2 ms. (b) Velocities in the radial direction in the IVS and PW obtained by 2D tracking.

the displacement in the lateral direction was different, and it was found that two yellow points in the interventricular septum overlapped, as shown in Fig. 15(a-2). In the present study, the characteristics of echoes were considered so that 2D motion could be estimated accurately at any position. The previous correlation kernel ($\alpha = 1.1$) could not provide an accurate estimation of the displacement at the boundary of the heart wall (p_0). On the other hand, the displacements in the lateral direction estimated using the proposed correlation kernel were in good agreement with typical heart wall motion.

5.4 Estimation of myocardial strain rate in radial direction

Figures 16(a) and 16(b) show the distributions of strain rate $S_r(r_i, \theta_j; n)$ and velocity $v_r(r_i, \theta_j; n)$ in the radial direction of the IVS and PW of the left ventricle around the R-wave. Low-pass filtering was applied to strain rate waveforms in the direction of the frame at a cutoff frequency of 86 Hz, because the effective components in the heart wall vibrations are known to be measured at frequencies less than 90 Hz.[5)]

Figures 16(a-1)–16(a-10) show the cross-sectional images of the short-axis view of the left ventricle (LV) obtained at intervals of 2 ms. Blue indicates thickening layer caused by myocardial contraction, and red indicates a thinning layer caused by myocardial relaxation. Roughly, it was found that IVS and PW moved complicately around the R-wave after the R-wave. These motions could not be observed by conventional speckle tracking because of the low frame rate of less than 50 Hz. At the beginning of the first heart sound, the myocardial contraction was found to begin at around the middle of the IVS and propagate along the IVS even during a very short period of 20 ms.

Figures 17(a) and 17(b) show the distributions of strain rates $\{S_r(r_i, \theta_j; n)\}$ and velocities $\{v_r(r_i, \theta_j; n)\}$ at every 2 ms in the radial direction between the end of the ejection period and the start of the second heart sound. The white curves in Fig. 17(a) indicate the manually identified positions where the polarities of the strain rates change. Roughly, in the ejection period, the LV contraction is associated with the downward displacement (to the posterior wall) in the IVS

 © 2012 The Japan Society of Applied Physics

Person-to-person distribution (up to 10 persons) by the author only. Not permitted for publication for institutional repositories or on personal Web sites.

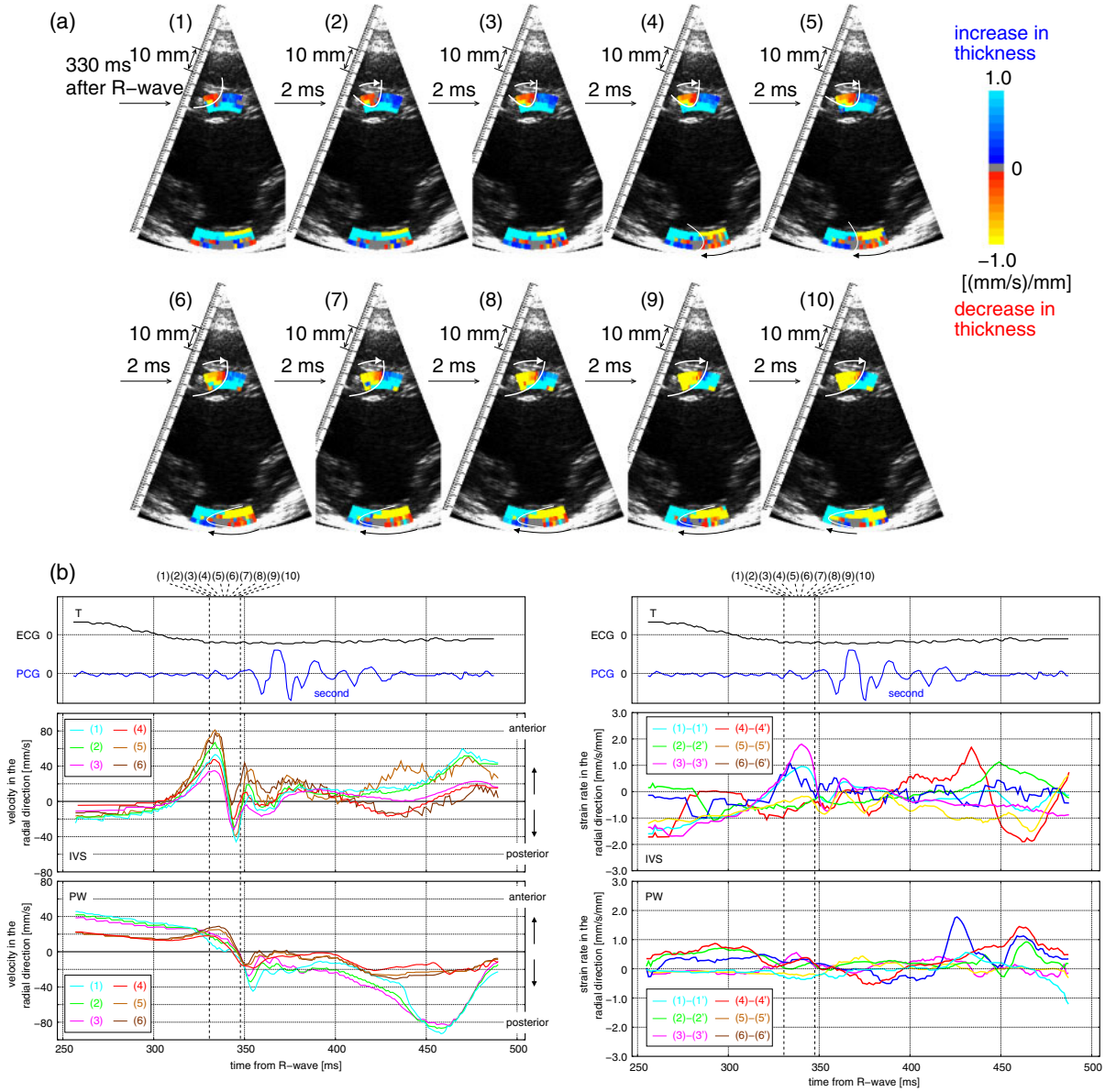

Fig. 17. (Color online) (a) Distributions of the strain rate in the radial direction around the second heart sound. The cross-sectional images of the short-axis view of left ventricle (LV) (1)–(10) were obtained every 2 ms. (b) Velocities in the radial direction in the IVS and PW obtained by 2D tracking.

and the upward displacement in the PW. As shown in Figs. 17(a-1)–17(a-10), the transition from contraction to relaxation was not spatially uniform, and propagated in the clockwise direction.

In this study, the velocities and strain rates in IVS and PW around the R-wave and the second heart sound could be observed at a high temporal resolution by the proposed method. These results indicate the potential of this method in the high-accuracy estimation of 2D velocities and strain rates and in detailed analyses of the physiological function of the myocardium.

6. Discussion and Conclusion

In this study, the optimal kernel sizes were determined in a phantom experiment with several SNRs and, then, the myocardial strain rate was estimated so that the myocardial function can be measured at a high frame rate. In a basic experiment of the determination of the optimal kernel size, the optimal sizes of the correlation kernel at depths $\{d\}$ of 20, 40, 60, and 80 mm were similar: in particular, SNRs were more than 15 dB. Moreover, it was found that the kernel size at the boundary must be set larger than that inside the wall. The optimal kernel sizes were seven times and four times the size of the PSF ($\Delta l(d) \times \Delta d(d)$) for the boundary region and inside the silicone rubber, respectively. To compare the optimal kernel size, which was determined in the phantom experiment, with other sizes, the radial strain rates estimated using different kernel sizes were examined using the normalized MSE of the estimated strain rate from the actual one obtained by the 1D phase-sensitive method. Compared with conventional kernel sizes, the proposed correlation kernel realized a more accurate measurement of the strain rate. However, even if the error between estimated and actual value is the minimum, corresponding to one sampling point, a 20% error of strain rate occurs [= (2.2 µm of sample spacing)/(12 µm of maximum instantaneous displacement)]. In future work, it is necessary to improve the spatial resolution and PSF should be made more narrow

 © 2012 The Japan Society of Applied Physics

Person-to-person distribution (up to 10 persons) by the author only. Not permitted for publication for institutional repositories or on personal Web sites.

by wringing the ultrasonic beam because the PSF, $(\Delta l \times \Delta d) = (2.48 \times 1.96)\,\mathrm{mm}^2$, at the depth d of 40 mm, was much larger than the instantaneous displacement of the silicone tube.

In the *in vivo* measurement, the regional instantaneous velocity and strain rate in the radial direction of the heart wall were measured at an extremely high temporal resolution (frame rate of about 860 Hz) without significant increase in the lateral spacing of scan lines (beam interval $\theta_s = 0.375°$). The estimated velocities of IVS and PW corresponded well with typical heart wall motion. Furthermore, the regional strain rate in the radial directions at IVS and PW around the R-wave and the second heart sound were analyzed in detail. Although the accuracy in estimation of strain rates should be further improved in future work to quantitatively assess the propagation speed of myocardial contraction/relaxation, the present results indicate the potential of this method in the high-accuracy estimation of strain rates and in detailed analyses of the transition in contraction and relaxation, which has not been measured by conventional tracking methods with a low temporal resolution.

Acknowledgment

This work was supported by a Grant-in-Aid for JSPS Fellows.

1) H. Kanai, H. Hasegawa, N. Chubachi, Y. Koiwa, and M. Tanaka: IEEE Trans. Ultrason. Ferroelectr. Freq. Control **44** (1997) 752.
2) J. D'hooge, B. Bijnens, J. Thoen, F. van de Werf, G. R. Sutherland, and P. Suetens: IEEE Trans. Med. Imaging **21** (2002) 1022.
3) G. R. Sutherland, G. D. Salvo, P. Claus, J. D'hooge, and B. Bijnens: J. Am. Soc. Echocardiogr. **17** (2004) 788.
4) H. Yoshiara, H. Hasegawa, H. Kanai, and M. Tanaka: Jpn. J. Appl. Phys. **46** (2007) 4889.
5) H. Kanai: IEEE Trans. Ultrason. Ferroelectr. Freq. Control **51** (2005) 1931.
6) S. Langeland, J. D'hooge, H. Torp, B. Bijnens, and P. Suetens: Ultrasound Med. Biol. **29** (2003) 1177.
7) L. N. Bohs, B. J. Geiman, M. E. Anderson, S. C. Gebhart, and G. E. Trahey: Ultrasonics **38** (2000) 369.
8) S. Langeland, J. D'hooge, T. Claessens, P. Claus, P. Verdonck, P. Suetens, G. R. Sutherland, and B. Bijnens: IEEE Trans. Ultrason. Ferroelectr. Freq. Control **51** (2004) 1537.
9) H. Geyer, G. Caracciolo, H. Abe, S. Wilandsky, S. Carerj, F. Gentile, H. J. Nesser, B. Khandheria, J. Narula, and P. P. Sengupta: J. Am. Soc. Echocardiogr. **23** (2010) 351.
10) J. D'hooge, E. Konofagou, F. Jamal, A. Heimdal, L. Barrios, B. Bijnens, J. Thoen, F. van de Werf, G. R. Sutherland, and P. Suetens: IEEE Trans. Ultrason. Ferroelectr. Freq. Control **49** (2002) 281.
11) B. Lind, J. Nowak, J. Dorph, J. van der Linden, and L.-A. Brodin: Eur. J. Echocardiography **3** (2002) 214.
12) Y. Notomi, P. Lysyansky, R. M. Setser, T. Shiota, Z. B. Popovic, M. G. Martin-Miklovic, J. A. Weaver, S. J. Oryszak, N. L. Greenberg, R. D. White, and J. D. Thomas: J. Am. Coll. Cardiol. **45** (2005) 2034.
13) T. H. Marwick, R. L. Leano, J. Brown, J. P. Sun, R. Hoffmann, P. Lysyansky, M. Becker, and J. D. Thomas: JACC: Cardiovasc. Imaging **2** (2009) 80.
14) I. Akiyama, A. Hayama, M. Nakajima, S. Yuta, and T. Itoh: Denshi Joho Tsushin Gakkai Ronbunshi D **J71-D** (1988) 733 [in Japanese].
15) K. Kaluzynski, X. Chen, S. Y. Emelianov, A. R. Skovoroda, and M. O'Donnell: IEEE Trans. Ultrason. Ferroelectr. Freq. Control **48** (2001) 1111.
16) L. N. Bohs, B. H. Friemel, B. A. McDermott, and G. E. Trahey: Ultrasound Med. Biol. **19** (1993) 751.
17) G. F. Pinton, J. J. Dahl, and G. E. Trahey: IEEE Trans. Ultrason. Ferroelectr. Freq. Control **53** (2006) 1103.
18) J. Bai, K. Liu, Y. Jiang, K. Ying, P. Zhang, and J. Shao: Ultrason. **48** (2008) 394.
19) F. Yeung, S. F. Levinson, and K. J. Parker: Ultrasound Med. Biol. **24** (1998) 427.
20) L. Cook, Y. Zhu, and T. J. Hall: Ultrasound Med. Biol. **29** (2003) S206.
21) S. Nakatani: GE Today (2003) p. 31.
22) Y. Honjo, H. Hasegawa, and H. Kanai: Jpn. J. Appl. Phys. **49** (2010) 07HF14.
23) R. F. Wagner, S. W. Smith, J. M. Sandrik, and H. Lopez: IEEE Trans. Sonics Ultrason. **30** (1983) 156.
24) I. Cespedes, Y. Huang, J. Ophir, and S. Spratt: Ultrason. Imaging **17** (1995) 142.
25) H. Hasegawa and H. Kanai: IEEE Trans. Ultrason. Ferroelectr. Freq. Control **55** (2008) 2626.
26) H. Kanai: Ultrasound Med. Biol. **35** (2009) 936.
27) W. Walker and G. E. Trahey: IEEE Trans. Ultrason. Ferroelectr. Freq. Control **42** (1995) 301.
28) S. B. Ramamurthy and G. E. Trahey: Ultrason. Imaging **13** (1991) 252.
29) D. Rappaport, D. Adam, P. Lysyansky, and S. Riesner: Ultrasound Med. Biol. **32** (2006) 1181.

 © 2012 The Japan Society of Applied Physics